Quantification of Cell Movement Reveals Distinct Edge

Motility Types During Cell Spreading

Benjamin J. Dubin-Thaler^[1], Jake M. Hofman^[2,3], Harry Xenias[1], Ingrid Spielman[1], Anna V. Shneidman[1], Lawrence A. David[4], Hans-Günther Döbereiner[1,2,5], Chris H. Wiggins[3], Michael P. Sheetz[1]*

^Equal Contributors
[1] Columbia University, Department of Biological Sciences, New York, NY, USA
[2] Columbia University, Department of Physics, New York, NY, USA
[3] Columbia University, Department of Applied Physics and Applied Math, New York, NY, USA
[4] Columbia University, Department of Biomedical Engineering, New York, NY, USA
[5] Universität Bremen, Institut für Biophysik, Bremen, Germany

*Corresponding author

Michael P. Sheetz, PhD
Department of Biological Sciences
Columbia University
Sherman Fairchild Center, Rm. 713
1212 Amsterdam Ave.
Mail Code 2408
New York, NY 10027
Tel: 212-854-4857
Fax: 212-854-6399
e-mail: ms2001@columbia.edu

Running title: Motility Types

Key words: image processing, computational methods, cell spreading, actin cytoskeleton, cell motility, cell adhesion

Characters (with spaces): 54,936

Abstract

Actin-based motility is central to cellular processes such as migration, bacterial engulfment, and cancer metastasis, and requires precise spatial and temporal regulation of the cytoskeleton. We studied one such process, fibroblast spreading, which involves three temporal phases: early, middle, and late spreading, distinguished by differences in cell area growth. In these studies, aided by improved algorithms for analyzing edge movement, we observed that each phase was dominated by a single, kinematically and biochemically distinct cytoskeletal organization, or *motility type*. Specifically, early spreading was dominated by periodic blebbing; continuous protrusion occurred predominantly during middle spreading; and periodic contractions were prevalent in late spreading. Further characterization revealed that each motility type exhibited a distinct distribution of the actin-related protein VASP, while inhibition of actin polymerization by cytochalasin D treatment revealed different dependences on barbed-end polymerization. Through this detailed characterization and graded perturbation of the system, we observed that although each temporal phase of spreading was dominated by a single motility type, in general cells exhibited a variety of motility types in neighboring spatial domains of the plasma membrane edge. These observations support a model in which global signals bias local cytoskeletal biochemistry in favor of a particular motility type.

Introduction

Actin-based cell motility plays a central role in diverse cellular processes such as the immune response (1, 2), wound healing (3), development (4, 5), and cancer metastasis (6, 7). While cytoskeletal motility depends on cellular context, the essential cytoskeletal proteins are conserved across eukaryotes (8) which may explain the observation of similar subcellular phenotypes, such as blebbing, ruffling and the formation of filopodia and lamellipodia across a broad range of cells, including mouse fibroblasts, endothelial cells, T-cells, neuronal cells, mammalian and amphibian epithelial cells, and drosophila wing-disk cells (9-13). We conjectured that these similarities in phenotype arise from a limited number of stable, underlying modes of cytoskeletal organization, or *motility types*, a claim supported by the observation that steady-state cell morphology also assumes a limited number of modes (14), and we performed a detailed characterization of motility types in a model cell type, the fibroblast, to contribute to a general understanding of how eukaryotic cytoskeletal components are organized and regulated.

A major difficulty in understanding the biochemistry and mechanics of the fibroblast cytoskeleton stems from the variety of forms and functions that these cells display. Just during migration, fibroblasts exhibit a combination of lamellipodial and filopodial based protrusion, retraction, and quiescence, complicating the identification of individual regulatory mechanisms. It has long been understood that "the spreading of cultured cells on the substratum may be regarded as a prototype of a major group of morphogenetic processes by which cells acquire non-spherical shapes and become attached to extracellular matrices," (15) and that cell spreading is a simple, physiologically-relevant method for isolating cytoskeletal behavior from the myriad of other cellular processes. Cell spread area as a function of time is well described by a sigmoid curve (16), and the spread area following the sigmoidal area increase is a widely used statistic for establishing the role a particular molecule or disease state plays in cytoskeletal regulation (17-21). Detailed light and electron microscope analyses have revealed that each temporal domain of the sigmoid corresponds to a distinct phase of spreading (22, 23), and previous quantitative computer analyses suggested that an abrupt change in edge kinematics correlated with the boundary between the second and third domain of the area sigmoid (24). Furthermore, we previously found that motility was highly uniform over the entire periphery of isotropically spreading cells (25). Thus, cell spreading provides an experimental system in which the normally heterogeneous cytoskeleton can be modeled by a progression of homogenous spreading phases.

To quantify the effects of experimental perturbations on cell spreading and migration, we used the edge *velocity map*, a method for generating a two-dimensional analog to the kymograph (13, 25). The velocity map is a plot of normal velocity as a function of of arc-length and time, where the normal velocity is defined to be the speed of edge movement in the direction normal to the edge. We can then use velocity maps as the basis for evaluating the kinematics of cell spreading over a variety of cell types and conditions (9, 11, 13, 24-27). Interestingly, the dynamics of the filopodial-rich neuronal growth cone (28) were found to be similar with those of filopodial-dominated, anisotropic spreading fibroblasts (25), underscoring the importance of quantitative image analysis in motility studies.

1   In this study we present kinematic, molecular, and pharmacological
2 characterizations of the phases of isotropic cell spreading and describe the three
3 fundamental motility types found within these phases: blebbing, continuous protrusion,
4 and periodic contractions. Each motility type correlates to a distinct localization of the
5 cytoskeletal protein VASP and responds differently to the inhibition of actin
6 polymerization by cytochalasin D. Our high resolution, global analysis of edge
7 movement reveals that each temporal spreading phase predominately exhibits a single
8 motility type, although spatial domains of varying motility types often occur
9 simultaneously. These findings provide evidence for a signaling hierarchy in which
10 locally defined motility types are coupled to global signals which enable the cell to
11 achieve particular functions.
12

Materials and Methods

Cell Culture and Sample Preparation

Immortalized mouse embryonic fibroblast cells were grown in Dulbecco's Modified Eagle Medium (DMEM) supplemented with 10% fetal bovine serum, 100 IU/ml of Penicillin-Streptomycin, 2 μM of L-Glutamine, and 2 μM of HEPES. All cultures were maintained at 37ºC in a 5% CO_2 incubator and cultures were never allowed to reach higher than 70% confluence. Culture reagents were purchased from Gibco-Invitrogen.

Spreading assays were performed as previously described (25). Briefly, cells were grown to 70% confluence, trypsinized briefly, washed with soybean trypsin inhibitor, centrifuged, and resuspended in phenol red and serum-free DMEM (Gibco-Invitrogen). Cells were then incubated for 20 minutes at 37ºC, followed by a second 20 minute incubation with 5 μM calcein red-orange-AM (Molecular Probes). Cells were then centrifuged and resuspended prior to plating.

Cover glasses were washed 2 h. in 20% nitric acid and exposed to gaseous 1,1,1,3,3,3-Hexamethyldisilazane (Sigma). We created a well on each cover glass using silicone isolators (Grace Bio-Labs, Inc.) and coated the hydrophobic, silanized cover glass with 600μL of a 10 μg/ml human plasma full-length pure fibronectin (Sigma) solution for 1 hour at 37ºC.

Cytochalasin D, Y-27632, and ML-7 were added to the cell suspension prior to plating for the time and concentration indicated. In all cases the concentration of these drugs was maintained throughout the spreading assay.

Microscopy

TIRF and bright-field time-lapse microscopy were performed as previously described (25). Cells were imaged with a 20X, 0.95NA water immersion objective (Olympus) on an Olympus BX-51 upright microscope. A custom stage was positioned above a stationary quartz dove prism (Edmund Scientific). Index of refraction matching immersion oil was added to the cover glass-prism interface. TIRF excitation was achieved using the 568nm emission from an argon-ion laser (Melles Griot) and passed through the prism at an angle of incidence at the cover glass-water interface of less than the critical angle to achieve total reflection, generating an evanescent wave approximately 100 nanometers into the sample medium. For bright field, the prism precluded the use of a condenser. A Cool Snap FX cooled CCD camera (Roper Scientific) controlled by SimplePCI (Compix Inc.) software was used to record the time-lapse micrographs.

Cell Motility Analysis Platform (CellMAP)

CellMAP is a suite of Matlab, Mathematica, and C/C++/ObjC command line programs designed to for the quantitative analysis of cell motility (13, 27). Input to CellMAP is any high contrast, time-lapse fluorescence sequence of a single cell whose boundary lies entirely within every frame of the sequence (Fig. 1b). Outputs include (but

are not limited to): arc-length-parameterized contours for each frame in the sequence, the
normal velocity of the cell edge as a function of space and time, the area of the cell as a
function of time, and a cross-correlation plot for the normal velocity as a function of arc-
length and time. The following details the calculations performed by CellMAP.

Segmentation and Normal Velocity Calculation (noVel)

The problem of cell segmentation for a time-lapse sequence of TIRF images can
be stated as follows: at each location i in a given frame we observe an image pixel h_i and
wish to infer the underlying scene pixel q_i, where $q_i \in \{+,-\}$ for pixels inside and outside
the cell, respectively. We work under a Gaussian noise model where, given the q_i's, the
h_i's are centered about class means $\mu_\pm$ with class standard deviations $\sigma_\pm$, all of which
must be inferred from the data. We assume all pixels are independent and identically
distributed, with no spatial coupling between class values at neighboring scene locations.

For each frame in the sequence we fit a two-component Gaussian mixture model
of the form

$$p(h_i) = \pi N(h_i; \mu_-, \sigma_-) + (1-\pi) N(h_i; \mu_+, \sigma_+) \tag{1}$$

to the distribution of pixel intensities (Fig. 1D) using Expectation Maximization, an
iterative, unsupervised learning algorithm (29). With the q_i's, $\mu_\pm$ and $\sigma_\pm$ now determined,
a time-dependent intensity threshold $\bar{h}(t)$ that satisfies

$$p(q_i = + | h = \bar{h}) = \alpha p(q_i = - | h = \bar{h}) \tag{2}$$

(for a user-specified α) is calculated. The inside of the cell is segmented from the
background and the resulting cell boundary $\Gamma(s,t)$ is parameterized by arc-length $s(t)$.

The normal velocity of each point on $\Gamma(s,t)$ is calculated from gradients of the
image data $h(\mathbf{x}(s,t),t)$ as

$$v_n = \frac{\partial_t (h(\mathbf{x},t) - \bar{h}(t))}{|\nabla h(\mathbf{x},t)|} \tag{3}$$

This is equivalent to the kinematic boundary condition in fluid dynamics and a simpler
case of the velocity inference problem often addressed by optical flow methods (30, 31).
The normal velocity as a function of arc-length and time is displayed in a color-coded
plot.

There are several advantages of the above method over previously employed
techniques (11, 25). Firstly, CellMAP automates cell segmentation, allowing for only one
user-controlled parameter, α, which has a mathematically principled and highly
interpretable origin: a pixel of intensity $\bar{h}(t)$ is α times as likely to have been drawn
from the foreground class than from the background class; α controls the "tightness" of
the contour. This parameter applies across all frames, removing uncertainties and
fluctuations introduced by manual thresholding of individual frames.

In addition, arc-length parameterization of the cell contour enables one to analyze the non-convex morphologies encountered in early spreading and highly polarized cells in which polar coordinate descriptions fail due to multi-valued $r(\theta,t)$ relations.

Finally, optical flow velocity calculation provides an accurate measure of the normal velocity for all points on the cell boundary. It should be noted that in highly anisotropic cells, the normal direction often differs dramatically from the radial direction; optical flow accurately captures normal velocity information for such cells via image gradients in a computationally-efficient manner without the need to explicitly construct local normal vectors.

Correlation Analysis

We employed a two-point correlation function to quantify the spatiotemporal patterns of protrusions and retractions in a cell. The discrete form of the correlation function is given by

$$c(\Delta t, \Delta s) = \frac{\sum_{t=1}^{T-\Delta t} \sum_{s=1}^{\max(S(t),S(t+\Delta t))} v(t,\mathrm{mod}(s,S(t))) * v(t+\Delta t,\mathrm{mod}(s+\Delta s,S(t+\Delta t)))}{(T-\Delta t) * \sum_{t=1}^{T} \max(S(t),S(t+\Delta t))} \qquad (4)$$

where $v(t,s)$ is the mean-subtracted membrane normal velocity as a function of arc-length s and time t, Δt is the lag in time, Δs is the lag in space, T is the maximum length of time in $v(t,s)$ and $S(t)$ is the total arc-length in $v(t,s)$ as a function of time. The modulus function, $\mathrm{mod}(x,X)$, is used in the spatial coordinate to establish periodic boundary conditions in the spatial dimension.

This correlation function compensates for changes in the total contour length as the cell increases and decreases in area. However, as it involves several explicit loops, it is also inherently computationally expensive. Therefore, we made use of the Wiener-Khinchin theorem that states that the auto-correlation function is equivalent to the inverse Fourier transform of the absolute value squared of the Fourier transform of a function. This approach was orders of magnitude faster due to the speed gained through using fast Fourier transform (FFT) algorithms on our discrete data. However, as FFT requires rectangular matrices as input, we sampled, via linear interpolation, a constant number of points along the contour with respect to time. The drawback of this approach is that one loses the ability to measure the spatial-lag in terms of arc-length. For P0 and P2, where the contour-length changes very little, we assigned the total length of the spatial-lag axis as the average arc-length of the cell in that phase. Comparison of results between the two-point and FFT based correlation functions were practically identical. For P1, where the total arc-length changes dramatically, length units are somewhat arbitrary and were simply scaled between 0 and 1. In all cases, the magnitude of the correlation function was normalized for unity at zero-lag.

1   *Results*

2   **Image Acquisition and Velocity Calculation**

3   We acquired time-lapse micrographs of isotropic spreading cells with both bright
4   field illumination (BF, Fig. 1A) and total internal reflection fluorescence (TIRF, Fig. 1B)
5   using a 20x objective (Movie S1). By exciting only fluorophores within 100nm of the
6   substrate (32), TIRF revealed membrane dynamics at the earliest spreading times that the
7   cell body usually obscures in bright field imaging (Fig. 1C). Using our Cell Motility
8   Analysis Package (CellMAP), we calculated the membrane edge position as a function of
9   arc-length and time (Fig. 1D) for each image in the TIRF sequence (Fig. 1E). We then
10   calculated the normal velocity of the cell edge as a function of arc-length and time (Fig.
11   1F, Movie S2) and performed correlation analyses on the velocity functions. (See
12   materials and methods for details of quantitative analyses.)

13   **Kinematic Signatures of Spreading Phases**

14   We previously observed that isotropic cell spreading can be divided into three
15   phases, early spreading (P0), middle spreading (P1), and late spreading (P2) (24), and
16   hypothesized that each phase represents changes in local cytoskeletal organization
17   (motility type) in response to larger scale regulatory signals (33). Fitting the logarithm of
18   cell area vs. time to a piecewise, linear function (Fig 2A), we identified each phase and
19   analyzed phase kinematics using CellMAP (Fig. 2B-D). We found that P0 exhibited
20   small, fast edge protrusions immediately followed by retraction (Fig. 2B), with velocities
21   ranging from -5 µm/min to 20µm/min. As previously reported (25), P1 was characterized
22   by a uniform protrusion of the cell edge (Fig. 2C). P2, the late spreading phase (Fig. 2D),
23   displayed a mixture of protrusion and retraction somewhat similar to P0 but with smaller
24   velocities, ranging from -2 to 4 µm/min. We previously reported and extensively
25   characterized myosin II dependent periodic lamellipodial contractions in P2 (9, 34).
26   However, by using a time resolution of two seconds between frames, less than half of the
27   five second average retraction time associated with a periodic contraction, we have
28   calculated the first high-resolution velocity maps of periodic contractions around the
29   entire cell edge. Although the range of velocities found in P0 and P2 were different, the
30   existence of alternating protrusion and retraction in both phases suggests the possibility
31   of a similar underlying mechanism between their dominant motility types.
32   In order to quantitatively compare the spatiotemporal organization of edge
33   velocity between P0 and P2, we calculated a 'two-point' auto-correlation function,
34   $c(\Delta t, \Delta s)$ for the velocity of the edge over space and time. The form of c for each
35   spreading phase (Fig. 3) reflects the average edge activity over that phase. To distinguish
36   between the different motility types, we used statistical measures from the correlation
37   plot to quantify both the spatial and temporal extent of motile activity as well as the
38   spatial and temporal spacing between regions of high activity. To illustrate, a plot of c for
39   simulated data is shown (Fig. S1).
40   Plotting c for P0 (Fig. 3A) revealed several features of interest within and
41   between phases. First, the average extent of an event in P0 was ~12 seconds (twice the
42   characteristic width of the peak at the origin in t) by ~6µm (twice the characteristic width
43   of the peak at the origin in s). Second, there was a periodicity between protrusion and

retractions as seen by repeated peaks and troughs in *c*, both on the *s=0* axis as well as off-axis. Periodicity on the *t* axis reveals a period of ~25 seconds for cycles of edge activity at a given position on the cell. The diagonal, off-axis lines of correlation indicate that activity propagates along the edge with a velocity of ~0.63 μm/s, a phenomenon which has been observed in a wide variety of cells (13). The correlation of P1 (Fig. 3B) shows the isotropic and continuous nature of motility in this phase (25), in contrast to the correlation plot for P2 (Fig. 3C). In P2, we observed a temporal extent of ~15 s., temporal oscillations with a period of ~18 s, and lateral propagation of ~1.5 μm/s. These measurements are similar to previous measurements of periodic contractions in spatially limited regions of the lamellipodium of P2 spreading and migrating cells (9, 24). In addition, our global analysis reveals a spatial extent of correlated activity of up to ~30 μm. Knowing that periodic contractions arise from a specific local organization of actin, myosin, and adhesions in the lamellipodium (34), and, intrigued by the similarities in period and lateral propagation between P2 and P0, we further investigated corresponding underlying cytoskeletal dynamics in these two phases.

P0 exhibits RHOK1 dependent membrane blebbing

In most cases, membrane movements in P0 could not be observed in BF because the cell body obscured the region of surface contact; however, in cases where the cell body was not directly above the site of initial contact, movements in the bright-field images were observed. These movements correlated to those observed in the velocity map and appeared to be extending and retracting membrane blebs (Fig. 4, Movie S3). While blebbing is a sign of apoptosis, it has also been reported in the early phase of cell spreading (23), mitosis (35), and migration (36). One mechanism for bleb formation is regulated by myosin light chain phosphorylation (37), a mechanism blocked by Rho kinase inhibitors (38-40). To test if the P0 blebbing we observed was governed by the same mechanism, we incubated the cells with 20μM of the Rho-kinase inhibitor Y-27632 for 30 minutes prior to spreading. Under these conditions, bleb formation was inhibited in all cells (n=125 cells). As in *Dictyostelium*, when blebbing was blocked, the basal stage was dominated by filopodial motility (41). Incubation with 20μM of the myosin light chain kinase inhibitor ML-7 did not inhibit bleb formation (n=30 cells), contrary to previous studies of apoptotic blebbing (42), suggesting that the action of MLCK and Rho-kinase may be spatially segregated in early spreading as in fully spread cells (43). Independent of the particular mechanism underlying blebbing in P0, these results clearly distinguished the P0 blebbing motility type from the P2 periodic contraction motility type that were inhibited by ML-7 and were associated with lamellipodial protrusion (9). These results also showed that while cells were predisposed to blebbing in P0, pharmacological intervention inhibiting this motility type left the sequence of isotropic spreading phases undisturbed, indicating that at least some of the elements regulating spreading phase were 'up-stream' of signals determining the motility type at the cell edge. In order to further explore the interdependence between motility types and spreading phase, we investigated molecules that would differentiate between motility types independent of spreading phase.

VASP localization provides a unique biochemical signature for each type of motility

VASP, a protein that binds both f-actin and adhesion proteins, is known to stimulate actin polymerization (44, 45), and has been observed both at the tip of the leading edge during periodic contractions as well as in rows of adhesions at the back of the lamellipodium following each contraction (9). We hypothesized that the organization of VASP would indicate molecular differences between different motility types.

Cells transiently transfected with VASP-GFP revealed that VASP was not concentrated at the tip of the protruding edge in the blebbing motility type (Fig. 5A). Instead, aggregates of VASP formed at the base of the bleb following bleb retraction. This suggested that VASP-dependent actin polymerization was not required for P0 bleb extension; however, VASP may form initial adhesions in P0 in response to bleb retraction, although we do not directly explore this relationship here. In P1, VASP in the protruding edge was above the region of fluorescence of our TIRF field (data not shown), requiring epifluorescence in order to visualize VASP. These observations revealed that VASP was localized at the tips of lamellipodia, although no VASP adhesion sites formed (Fig. 5B). In P2, we observed VASP during periodic contractions at the cell edge (Fig. 5C, left) consistent with previous observations (9). However, we also observed transitions from periodic contraction motility to continuous protrusion motility with VASP distribution (Fig. 5C, right, Movie S4) similar to that in continuous protrusion during P1 (Fig. 5B). These results indicated that VASP distribution is different in each of the spreading motility types. Further, since both continuous lamellipodial extension and periodic contractions occur simultaneously in P2 (Fig. 5C, Movie S4) and P1 cells can exhibit spatially limited regions of motility types at the same time as continuous protrusion (Fig. 2C), we suggest that mixing between motility types is a general phenomenon.

Effects of Cytochalasin D depend on motility type

To explore the polymerization complexes involved in the different phases of cell spreading, we treated cells with the barbed end binding toxin cytochalasin D (CD) over a range of concentrations (0nM, 30 nM, 60 nM, 100 nM, and 200 nM) for 30 minutes prior to spreading, and analyzed 11, 10, 12, 5, and 8 spreading cells over two trials for each condition, respectively. We generated edge velocity maps for these cells and selected the isotropic spreading cells from the total population for further study (Fig. 7A, Fig. S2). Transitions between phases, defined by changes in the rate of area change (see above), were distinguishable at up to 100 nM of CD, although increased CD concentration disrupted the spatiotemporal organization of motility types and decreased the final spread extent of cells. These results suggested that the mechanism of transition between phases is relatively insensitive to barbed end inhibition by CD, similar to the above finding that altering the motility type of P0 with Rho kinase inhibitor does not effect the P0-P1 transition.

To quantify the effect of CD on different motility types, we analyzed the distributions of velocities from all cells at a given CD concentration in a specific phase (Fig. 7B-D). Each distribution was fit to a Gaussian mixture model, a linear combination of several Gaussian components, each specified by three parameters; μ (mean), σ (standard deviation), and π (relative weight). Each component of the mixture model

1   represented a particular underlying motility mechanism - quiescence, bleb protrusion,
2   bleb retraction, or continuous extension - and μ, σ, and π characterized the edge
3   kinematics of each mechanism.
4   We used a three-component mixture model to describe P0, reflecting that this
5   spreading phase was comprised of a combination of barbed end independent motility
6   (blebbing), a barbed end dependent motility, and quiescence. The high-velocity Gaussian
7   component corresponded to the high-velocity bleb protrusion events, and the speed of
8   these protrusions changed by a relatively small amount across the range of CD
9   treatments, from 10 μm/min to 8 μm/min (Fig. 7B & E). The low-velocity Gaussian
10 component in P0 revealed a population of protrusion events with a velocity distribution
11 centered at 4μm/min under control conditions that shifted to 1μm/min at 100nM CD. The
12 final Gaussian component represented the quiescent regions of the cell whose velocity
13 remained unchanged with CD treatment.
14   We also used three-component Gaussian mixture model for the velocities in P1.
15 One component modeled the quiescent regions of the cell for each treatment, with the
16 exception of control cells where there were few quiescent regions in P1. The other two
17 Gaussian components modeled the distribution of velocities in continuously protruding
18 regions of the cell. The mean velocities of both components of the continuous protrusion
19 motility type decreased at higher CD concentrations, although the most dramatic decrease
20 was in the fraction of the edge exhibiting these high velocities. Indeed, as CD treatment
21 increased, the probability of a given part of the cell being quiescent (π_1) increased. There
22 was an abrupt shift at 60 nM CD (Fig. 7C,F), indicating that at this concentration of CD a
23 pool of excess barbed ends was finally eliminated by CD barbed end capping.
24 Furthermore, the observation that a given part of the cell either exhibited the continuous
25 protrusion motility type *or* quiescence supports our hypothesis that each motility type
26 represents a discrete state of cytoskeleton organization.
27   To further quantify the disruption of the organization of motility types by CD, we
28 applied correlation analyses. Analysis of P0 (Fig. 7B) revealed the least disruption of
29 spatiotemporal patterning – the blebbing motility type was essentially unchanged by
30 increasing [CD]. P1 motility, however, underwent a substantial shift in organization;
31 while cells continued to exhibit highly correlated spatial regions of persistent activity,
32 instead of a single, spatially connected region of spreading, correlation maps revealed
33 cells that exhibited multiple isolated spatial domains of high correlation (Fig. 7C, left,
34 middle). In general, the spatial extent of correlation decreased as CD was added (Fig. 7C,
35 right). These results suggest that while P1 promotes continuous protrusion, the presence
36 of CD decreases the probability for continuous protrusion of the cytoskeleton in a given
37 local region of the cell due to decreasing barbed-end availability.

Motility Types in Polarization

39   Polarization and migration require the cell to bias net-protrusive motility types in
40 one region while motility types giving a net-retraction must occur in a diametrically
41 opposed region. Cell spreading is often an isotropic process and the mechanism by which
42 a cell transitions into a polarized and migratory state is not well understood. It was
43 recently observed that PKCθ is required for the maintenance of polarity and migration in
44 T-cells. In cells lacking PKCθ, the lateral propagation of activity was unchecked,
45 preventing cells from forming a stable cell front and moving in a directed manner (Simms

1   et al.). In P2 fibroblasts, spatially isolated regions of periodic contractions also exhibited
2   lateral propagation at a rate of 0.375 µm/s, (Fig. 7 A, B). However, as time progressed,
3   the rate of this propagation greatly decreased (Fig. 7 C), and this suppression of lateral
4   propagation of edge activity may represent an important step in developing cell polarity.

Discussion

Isotropic cell spreading is a process during which a cell exhibits a small number of motility types in coordination with two sharp transitions in global behavior. These changes in global behavior correspond to abrupt changes in slope in the plot of spread area versus time. Detailed characterization of the spreading motility types reveals that they are similar to those observed during more general phenomena. For instance, cells can exhibit membrane blebbing during mitosis (35), during development (46, 47), and during cancer cell movement (36, 48). Motility very similar to P1 continuous spreading has been observed in post-mitotic cell spreading (Gauthier et al., in submission) and keratocyte migration, as well as in tumor-derived epithelial cell lines acutely exposed to epidermal growth factor, which undergo a two minute long period of rapid actin polymerization (49). Furthermore, we show that P2 cells exhibit global periodic contractions, one of the most fully understood motility types in migrating cells (9). Thus, the quantitative characterization of spreading motility types can provide an important aid in building models of the mechanisms of movement in vivo (50) as well as a tool for evaluating the specific effect of perturbations such as siRNA knockdown (26) or a particular disease state such as oncogenic mutation. Using kinematic (Fig. 1-3) and molecular (Fig. 5) fingerprints for the different motility types combined with an understanding of the molecular machines that contribute to those motility types (34, 39, 51), one can deduce the molecular-level function of a perturbation based on our relatively low resolution, high-throughput, quantitative spreading assay. Such an approach could provide fast, highly interpretable functional screens for chemical libraries, siRNA libraries, or tumor cells.

Spreading assays owe their interpretability to the discrete nature of motility types. Not only are the temporal transitions between phases very sharp, but the spatial boundaries between two different motility types are equally abrupt. For instance, in P1, some cells contained regions where they did not exhibit continuous spreading. Instead of observing a gradual decrease in the speed of edge protrusion into a quiescent region, the boundary between the regions of continuous protrusion and these regions were very abrupt. In addition, in response to a range of concentrations of cytochalasin D (Fig. 6), we observed intermediate states between uninhibited continuous protrusion and complete inhibition. In these intermediate states, we observed that, while the velocities of regions of the cell still exhibiting continuous protrusion exhibit a mild dependence on CD, the regions of the cell with no suppressed or different motility types entirely increased dramatically. Thus we conclude that continuous spreading is a stable state in the organization of the cytoskeleton and that reducing barbed ends inhibits this state, resulting in fewer regions of the cell that exhibit continuous protrusion in the presence of CD. Both periodic contractions and blebbing motility exhibit a similar, discrete nature. Interestingly, even in cells where the organization of continuous spreading was highly disrupted, abrupt changes in spreading phase associated with global changes in motility type were still observed.

Together, these results support our proposed model of hierarchical motility regulation (33). At the lowest level of the hierarchy are actin and proteins that directly modify actin dynamics (e.g., actin polymerization factors VASP or WAVE, actin

nucleators such as Arp2/3, depolymerization factors such as cofilin) and their immediate regulatory molecules (e.g., Abl, LIMK1), responsible for directly determining the motility type in a local region of the cell. A particular organization of these molecules gives rise to a stereotypic kinematic signature of the cell edge, as a result of a particular balance of actin polymerization, adhesion formation, myosin activity, filament cross linking, and any number of other processes that alter the local cytoskeletal environment. At the higher levels of the hierarchy are molecules that lead to global organizational changes such as those observed in transitions between spreading phases. Candidate molecules are the Rho family GTPases (52) or calcium signals induced by integration of chemical or mechanical signals (53), and we propose that such global signals influence the probability that a given motility type is activated on a regional or global scale. This hypothesis of modular, hierarchical control of the cytoskeleton provides a framework by which multiple higher-level signals are integrated to contribute to the overall motile function. The specific type of edge motility activated in a given region of a cell depends upon both global and local signals; indeed, switching between migrational modes has been observed in neurons (54, 55), amoeba (41), and in the immune synapse (56), and in tumor cells (36, 55, 57).

This hierarchy of locally defined motility types combined with global regulation allows an evolutionary independence between low-level cytoskeletal function, which is highly conserved, and the regulation of global cellular function, which is highly divergent. Flexibility, evolvability, and non-linearity are properties of a variety of evolved systems, and these properties are readily achieved through hierarchical organization (58). For example, the modular nature of genes in which cis-regulatory sequences and protein coding sequences are independently altered through evolutionary processes results in the potential for the development of complex spatial and temporal expression patterning while using similar fundamental protein building blocks (59). In this case, evolutionarily-conserved motility types play a role analogous to the expressed proteins while global motility regulatory signals play a role analogous to the cis-regulatory elements, giving the cell the ability to use the same low-level motility machinery to carry out diverse functions depending on the specific cellular context.

In a recent editorial on the state of systems biology, George Church asks how the rest of biology can "reach the enviable status of bioinformatics and crystallography?" and suggests that sharing data is a crucial step towards achieving this goal (60). All data for the cells analyzed in this paper, along with their corresponding two-dimensional velocity maps and the open source software CellMAP, are available at http://cellmap.sourceforge.net. In the spirit of projects such as the Open Microscopy Project (http://www.openmicroscopy.org), we hope that making our data and software freely available will provide a model for a collaborative future in the field of cell motility and guide the way to a more systematized approach for storing and distributing cell imaging data, such as already exists in the fields of protein biophysics.

Acknowledgements

The authors thank Greg Giannone and the entire Sheetz Lab for their stimulating conversations and criticisms and Greg Neumann and Maria Zuber (NASA) for providing the color scale used in the velocity plots. This work was supported by the NIH and the NSF.

Abbreviations list

CD .... cytochalasin D
CellMAP .... cell motility analysis package
P0 .... early spreading phase
P1 .... fast spreading phase
P2 .... late spreading phase
TIRF .... total internal reflection fluorescence

References

1.   Dustin, M. L., P. M. Allen, and A. S. Shaw. 2001. Environmental control of immunological synapse formation and duration. Trends in Immunology 22:192-194.
2.   Friedl, P., A. T. den Boer, and M. Gunzer. 2005. TUNING IMMUNE RESPONSES: DIVERSITY AND ADAPTATION OF THE IMMUNOLOGICAL SYNAPSE. Nature Reviews Immunology 5:532-545.
3.   Singer, A. J., and R. A. Clark. 1999. Cutaneous wound healing. The New England journal of medicine 341:738-746.
4.   Baum, B. 2004. Animal Development: Crowd Control. Current Biology 14:R716-R718.
5.   Winklbauer, R., and A. Selchow. 1992. Motile behavior and protrusive activity of migratory mesoderm cells from the Xenopus gastrula. Dev Biol 150:335-351.
6.   Condeelis, J., R. H. Singer, and J. E. Segall. 2005. THE GREAT ESCAPE: When Cancer Cells Hijack the Genes for Chemotaxis and Motility. Annual Review of Cell and Developmental Biology 21:695-718.
7.   Kaplan, R. N., R. D. Riba, S. Zacharoulis, A. H. Bramley, L. Vincent, C. Costa, D. D. MacDonald, D. K. Jin, K. Shido, S. A. Kerns, Z. Zhu, D. Hicklin, Y. Wu, J. L. Port, N. Altorki, E. R. Port, D. Ruggero, S. V. Shmelkov, K. K. Jensen, S. Rafii, and D. Lyden. 2005. VEGFR1-positive haematopoietic bone marrow progenitors initiate the pre-metastatic niche. Nature 438:820-827.
8.   Pollard, T. D. 2003. The cytoskeleton, cellular motility and the reductionist agenda. Nature 422:741-745.
9.   Giannone, G., B. J. Dubin-Thaler, H. G. Dobereiner, N. Kieffer, A. R. Bresnick, and M. P. Sheetz. 2004. Periodic lamellipodial contractions correlate with rearward actin waves. Cell 116:431-443.
10.   Medeiros, N. A., D. T. Burnette, and P. Forscher. 2006. Myosin II functions in actin-bundle turnover in neuronal growth cones. Nat Cell Biol 8:215-226.
11.   Machacek, M., and G. Danuser. 2006. Morphodynamic profiling of protrusion phenotypes. Biophys J 90:1439-1452.
12.   Silva, H. S., M. L. Martins, M. J. Vilela, R. Jaeger, and B. Kachar. 2006. 1/f ruffle oscillations in plasma membranes of amphibian epithelial cells under normal and inverted gravitational orientations. Phys Rev E Stat Nonlin Soft Matter Phys 74:041903.
13.   Döbereiner, H. G., B. J. Dubin-Thaler, J. M. Hofman, H. S. Xenias, T. N. Sims, G. Giannone, M. L. Dustin, C. H. Wiggins, and M. P. Sheetz. 2006. Lateral membrane waves constitute a universal dynamic pattern of motile cells. Phys Rev Lett 97:038102.
14.   Heo, W. D., and T. Meyer. 2003. Switch-of-function mutants based on morphology classification of Ras superfamily small GTPases. Cell 113:315-328.
15.   Vasiliev, J. M. 1982. Spreading and locomotion of tissue cells: factors controlling the distribution of pseudopodia. Philos Trans R Soc Lond B Biol Sci 299:159-167.
16.   Bardsley, W. G., and J. D. Aplin. 1983. Kinetic analysis of cell spreading. I. Theory and modelling of curves. J Cell Sci 61:365-373.
17.   Price, L. S., J. Leng, M. A. Schwartz, and G. M. Bokoch. 1998. Activation of Rac and Cdc42 by integrins mediates cell spreading. Mol Biol Cell 9:1863-1871.

18.   de Hoog, C. L., L. J. Foster, and M. Mann. 2004. RNA and RNA binding proteins participate in early stages of cell spreading through spreading initiation centers. Cell 117:649-662.

19.   Adamsky, K., J. Schilling, J. Garwood, A. Faissner, and E. Peles. 2001. Glial tumor cell adhesion is mediated by binding of the FNIII domain of receptor protein tyrosine phosphatase beta (RPTPbeta) to tenascin C. Oncogene 20:609-618.

20.   Tamura, M., J. Gu, K. Matsumoto, S. Aota, R. Parsons, and K. M. Yamada. 1998. Inhibition of cell migration, spreading, and focal adhesions by tumor suppressor PTEN. Science 280:1614-1617.

21.   von Wichert, G., G. Jiang, A. Kostic, K. De Vos, J. Sap, and M. P. Sheetz. 2003. RPTP-alpha acts as a transducer of mechanical force on alphav/beta3-integrin-cytoskeleton linkages. J Cell Biol 161:143-153.

22.   Bliokh Zh, L., and V. V. Smolianinov. 1977. [Kinetics of fibroblast spreading]. Biofizika 22:281-288.

23.   Bereiter-Hahn, J., M. Luck, T. Miebach, H. K. Stelzer, and M. Voth. 1990. Spreading of trypsinized cells: cytoskeletal dynamics and energy requirements. J Cell Sci 96 (Pt 1):171-188.

24.   Döbereiner, H. G., B. Dubin-Thaler, G. Giannone, H. S. Xenias, and M. P. Sheetz. 2004. Dynamic phase transitions in cell spreading. Phys Rev Lett 93:108105.

25.   Dubin-Thaler, B. J., G. Giannone, H. G. Dobereiner, and M. P. Sheetz. 2004. Nanometer analysis of cell spreading on matrix-coated surfaces reveals two distinct cell states and STEPs. Biophys J 86:1794-1806.

26.   Cai, Y., N. Biais, G. Giannone, M. Tanase, B. Ladoux, J. Hofman, C. H. Wiggins, and M. P. Sheetz. 2006. Nonmuscle Myosin IIA-dependent Force Inhibits Cell Spreading and Drives F-actin Flow. Biophys J.

27.   Ada-Nguema, A. S., H. Xenias, M. P. Sheetz, and P. J. Keely. 2006. The small GTPase R-Ras regulates organization of actin and drives membrane protrusions through the activity of PLCepsilon. J Cell Sci 119:1307-1319.

28.   Betz, T., D. Lim, and J. A. Kas. 2006. Neuronal Growth: A Bistable Stochastic Process. Physical Review Letters 96:098103-098104.

29.   Hastie, T. 2001. The elements of statistical learning : data mining, inference, and prediction. Springer, New York.

30.   Weiss, Y., and D. J. Fleet. 2000. Velocity likelihoods from generative models. Invest Ophth Vis Sci 41:S795-S795.

31.   Poggio, T., V. Torre, and C. Koch. 1985. Computational Vision and Regularization Theory. Nature 317:314-319.

32.   Axelrod, D., N. L. Thompson, and T. P. Burghardt. 1983. Total internal inflection fluorescent microscopy. J Microsc 129 Pt 1:19-28.

33.   Döbereiner, H. G., B. J. Dubin-Thaler, G. Giannone, and M. P. Sheetz. 2005. Force sensing and generation in cell phases: analyses of complex functions. J Appl Physiol 98:1542-1546.

34.   Giannone, G., B. J. Dubin-Thaler, O. Rossier, Y. Cai, O. Chaga, G. Jiang, W. Beaver, H. G. Dobereiner, Y. Freund, G. Borisy, and M. P. Sheetz. 2007. Lamellipodial actin mechanically links Myosin activity with adhesion-site formation. Cell 128:561-575.

35.   Boss, J. 1955. Mitosis in cultures of newt tissues. IV. The cell surface in late anaphase and the movements of ribonucleoprotein. Exp Cell Res 8:181-187.

36.   Sahai, E., and C. J. Marshall. 2003. Differing modes of tumour cell invasion have distinct requirements for Rho/ROCK signalling and extracellular proteolysis. Nat Cell Biol 5:711-719.

37.   Mills, J. C., N. L. Stone, J. Erhardt, and R. N. Pittman. 1998. Apoptotic membrane blebbing is regulated by myosin light chain phosphorylation. J Cell Biol 140:627-636.

38.   Sebbagh, M., C. Renvoize, J. Hamelin, N. Riche, J. Bertoglio, and J. Breard. 2001. Caspase-3-mediated cleavage of ROCK I induces MLC phosphorylation and apoptotic membrane blebbing. Nat Cell Biol 3:346-352.

39.   Charras, G. T., J. C. Yarrow, M. A. Horton, L. Mahadevan, and T. J. Mitchison. 2005. Non-equilibration of hydrostatic pressure in blebbing cells. Nature 435:365-369.

40.   Coleman, M. L., E. A. Sahai, M. Yeo, M. Bosch, A. Dewar, and M. F. Olson. 2001. Membrane blebbing during apoptosis results from caspase-mediated activation of ROCK I. Nat Cell Biol 3:339-345.

41.   Yoshida, K., and T. Soldati. 2006. Dissection of amoeboid movement into two mechanically distinct modes. J Cell Sci 119:3833-3844.

42.   Barros, L. F., T. Kanaseki, R. Sabirov, S. Morishima, J. Castro, C. X. Bittner, E. Maeno, Y. Ando-Akatsuka, and Y. Okada. 2003. Apoptotic and necrotic blebs in epithelial cells display similar neck diameters but different kinase dependency. Cell death and differentiation 10:687-697.

43.   Totsukawa, G., Y. Wu, Y. Sasaki, D. J. Hartshorne, Y. Yamakita, S. Yamashiro, and F. Matsumura. 2004. Distinct roles of MLCK and ROCK in the regulation of membrane protrusions and focal adhesion dynamics during cell migration of fibroblasts. J Cell Biol 164:427-439.

44.   Bear, J. E., T. M. Svitkina, M. Krause, D. A. Schafer, J. J. Loureiro, G. A. Strasser, I. V. Maly, O. Y. Chaga, J. A. Cooper, G. G. Borisy, and F. B. Gertler. 2002. Antagonism between Ena/VASP proteins and actin filament capping regulates fibroblast motility. Cell 109:509-521.

45.   Mejillano, M. R., S. Kojima, D. A. Applewhite, F. B. Gertler, T. M. Svitkina, and G. G. Borisy. 2004. Lamellipodial versus filopodial mode of the actin nanomachinery: pivotal role of the filament barbed end. Cell 118:363-373.

46.   Fujinami, N., and T. Kageyama. 1975. Circus movement in dissociated embryonic cells of a teleost, Oryzias latipes. J Cell Sci 19:169-182.

47.   Kageyama, T. 1977. MOTILITY AND LOCOMOTION OF EMBRYONIC CELLS OF THE MEDAKA, ORYZIAS LATIPES, DURING EARLY DEVELOPMENT. Development, Growth & Differentiation 19:103-110.

48.   Keller, H. U., and H. Bebie. 1996. Protrusive activity quantitatively determines the rate and direction of cell locomotion. Cell Motil Cytoskeleton 33:241-251.

49.   Bailly, M., J. S. Condeelis, and J. E. Segall. 1998. Chemoattractant-induced lamellipod extension. Microsc Res Tech 43:433-443.

50.   Chamaraux, F., S. Fache, F. Bruckert, and B. Fourcade. 2005. Kinetics of cell spreading. Phys Rev Lett 94:158102.

51.   Sawada, Y., M. Tamada, B. J. Dubin-Thaler, O. Cherniavskaya, R. Sakai, S. Tanaka, and M. P. Sheetz. 2006. Force sensing by mechanical extension of the Src family kinase substrate p130Cas. Cell 127:1015-1026.

52.   Vial, E., E. Sahai, and C. J. Marshall. 2003. ERK-MAPK signaling coordinately regulates activity of Rac1 and RhoA for tumor cell motility. Cancer cell 4:67-79.

53.   Munevar, S., Y. L. Wang, and M. Dembo. 2004. Regulation of mechanical interactions between fibroblasts and the substratum by stretch-activated Ca2+ entry. J Cell Sci 117:85-92.

54.   Ayala, R., T. Shu, and L. H. Tsai. 2007. Trekking across the brain: the journey of neuronal migration. Cell 128:29-43.

55.   Marin, O., M. Valdeolmillos, and F. Moya. 2006. Neurons in motion: same principles for different shapes? Trends Neurosci 29:655-661.

56.   Friedl, P., A. T. den Boer, and M. Gunzer. 2005. Tuning immune responses: diversity and adaptation of the immunological synapse. Nat Rev Immunol 5:532-545.

57.   Wang, W., J. B. Wyckoff, S. Goswami, Y. Wang, M. Sidani, J. E. Segall, and J. S. Condeelis. 2007. Coordinated regulation of pathways for enhanced cell motility and chemotaxis is conserved in rat and mouse mammary tumors. Cancer research 67:3505-3511.

58.   Kirschner, M., and J. Gerhart. 2005. The plausibility of life : resolving Darwin's dilemma. Yale University Press, New Haven.

59.   Wittkopp, P. J. 2006. Evolution of cis-regulatory sequence and function in Diptera. Heredity 97:139-147.

60.   Church, G. M. 2005. From systems biology to synthetic biology. Mol Syst Biol 1:2005 0032.

1 *Figure legends*

2 **Figure 1: The velocity map encapsulates the kinematics of cell spreading**

3 (A) Bright field sequence of a mouse embryonic fibroblast spreading on a fibronectin coated
4 cover glass. Each image is 62μm high and there is 1 minute between each frame. (B) Same as A
5 except with total internal reflection fluorescence (TIRF) illumination. TIRF reveals only the
6 regions of the cell in closest contact with the surface, allowing for the visualization of edge
7 dynamics at the earliest times. (C) Merge of bright field (red) and TIRF (green) sequences. The
8 cell edge in bright field exactly matches the cell edge in TIRF. (D) Example of Gaussian mixture
9 modeling and expectation-maximization method for image segmentation of a TIRF image (left).
10 A mixture of two Gaussian distributions is used to fit the pixel intensity histogram (middle),
11 where one Gaussian models background pixels and one models pixels corresponding to our
12 fluorescent signal. A threshold is determined by tuning the relative probability that a given pixel
13 intensity belongs to the background or signal distributions (right). The only free parameter in this
14 calculation, performed by a convergent expectation-maximization algorithm, is α, the tightness
15 factor. Two different values of α result in two different values for the threshold, h_1 and h_2. (E)
16 Segmentation of the sequence of TIRF images in B for constant α. (F) The sequence of contours
17 gives edge position as a function of arc-length and time (left). The edge position is then used to
18 determine the points at which to calculate a 3D optical flow from the original image data
19 (middle). The velocity surface is plotted over arc-length and time (right). The cell analyzed in
20 this figure corresponds to cell 646 in the database.

21 **Figure 2: Each spreading phase exhibits a unique kinematic signature**

22 (A) The time domains of different phases are determined by the best fit of a 3-regime, piecewise
23 function to the logarithm of the area curve (left). These domains are then used to divide the
24 velocity map into different regions (middle). The three phases have distinct normal velocity
25 distributions (right). (B) Phase 0 spreading. Sequence of TIRF images (left) with an interval of 6
26 seconds. Velocity map (middle). Velocity histogram (right). (C) Phase 1 spreading. Sequence of
27 TIRF images (left) with an interval of 14 seconds. Velocity map (middle). Velocity histogram
28 (right). (D) Phase 2 spreading. Sequence of TIRF images (left) with an interval of 14 seconds.
29 Velocity map (middle). Velocity histogram (right). Scale bars represent 10μm. The cell analyzed
30 corresponds to ID 646 in the database.

31 **Figure 3: Auto-correlation functions reveal different characteristic lengths**
32 **and periods in each phase**

33 Two-point correlation function, $c(\Delta t, \Delta s)$ applied to velocity maps reveal patterns of membrane
34 movement for P0 (A), P1 (B) and P2 (C). Correlation density maps reveal overall patterns (left
35 column) while plots of the $\Delta t = 0$ or $\Delta s = 0$ sections (right column) illustrate temporal and spatial
36 features alone. The width of the first peak in c around the origin gives the average feature size in
37 time and arc-length for each phase. The distance to the first maximum in the time axis gives the
38 average temporal periodicity of the velocity plot. The distance to the first maximum in the space
39 axis gives the average periodicity in space. Diagonals in the correlation plots reveal lateral
40 propagation of active regions, particularly evident in the P0 plot. Arc-length in P1 is expressed
41 with respect to the maximum arc-length, S, because S(t) is changing rapidly in this phase.
42 Database ID for (A) and (B) is 646, (C) corresponds to ID 625.

Figure 4: Periodic protrusion and retraction in the basal phase is a result of blebs

(A) Bright field (left), TIRF (middle) and merge (right) images of a cell exhibiting blebbing motility (arrow indicates a region of blebbing) during P0. Scale bar is 10μm. (B) Velocity map of the same cell where the dashed lines indicates the time points represented by the images in (A). The blebs observed in bright field correspond to the regions of patches of protrusion in the velocity map. Cell database ID = 643.

Figure 5: VASP localization acts as a molecular marker to differentiate between the different phases of spreading

(A) A TIRF time sequence of VASP localization reveals that the protein is not enriched at the tips of P0 blebs during protrusion though VASP localizes in adhesions that form following bleb protrusion. (B) During P1, epifluorescence reveals that VASP is concentrated at the leading edge of continuous protrusion, as indicated by a line plot of intensity. The dashed line indicates the region over which the line plot was taken. (C) When the cell enters P2, periodic contractions can occur, with VASP at the tip of the protrusion as well as in rows of adhesions (left). However, the edge can switch back to a continuous protrusion (C, right), at which point VASP is again localized only at the tip, identical to continuous protrusion in P1. Scale bars represent 10μm.

Figure 6: Effect of CD on edge velocity during isotropic cell spreading

(A) Velocity maps of representative isotropic cells plated following 30 minute incubation with the indicated concentration of CD reveal that motility in P2 is most readily disrupted, followed by P1, with P0 blebbing motility being the least sensitive to CD. Cell ID in database, listed from low to high [CD]: 625, 649 641, 655, 612. (B-D) Velocity histograms for all cells treated with the indicated concentration of CD for P0 (B) P1 (C) and P2 (D). Overlay of a three-component Gaussian mixture model illustrates that different motility types correspond to different combinations of peaks in the velocity distribution. The ith Gaussian component has three parameters, μ_i, σ_i, and π_i, corresponding to the mean, standard deviation, and weight of that component, respectively. CD treatment, while capable of changing the velocity of a particular type of motility (reflected in changes to μ for the corresponding Gaussian component), also alters the probability that a given section of the cell will be in that particular type of motility (reflected in changes to π). (E-F) Summary of the values of μ and π vs. [CD] for the three different Gaussian components in P0 (E) and P1 (F) reveal differences in the dependence on barbed ends for different types of motility. While the velocity of continuous protrusion in P1 decreases with increasing CD (μ_1 in F, left panel), the fraction of the cell that exhibits continuous protrusion (represented by the increasing π_1 and decreasing π_2 π_3 in F, right panel) decreases as the quiescent fraction increases (π_1). (G) Correlation maps of P0 vs. [CD] show that CD does not disrupt the spatiotemporal organization of blebbing. Cell ID's are same as in A. (H) 2-D (left) and 1D (middle) correlation plots for a P1 for a cell treated with 60nM CD exhibited multiple regions of high correlation (Cell ID 631). In general, the extent of high correlation decreases with increasing [CD] (right), indicating that the extent of regions undergoing continuous protrusion is decreasing.

Figure 7: Laterally propagating domains of periodic contractions

(A) After entering P2, some cells exhibit a lateral propagation of regions exhibiting periodic contractions. This large-scale lateral propagation is seen by correlation analysis (B) performed in the region of the velocity map indicated by the dashed grey lines. After 8 minutes, the speed of lateral propagation decreases (C). The suppression of lateral propagation may be an important step in establishing polarization.
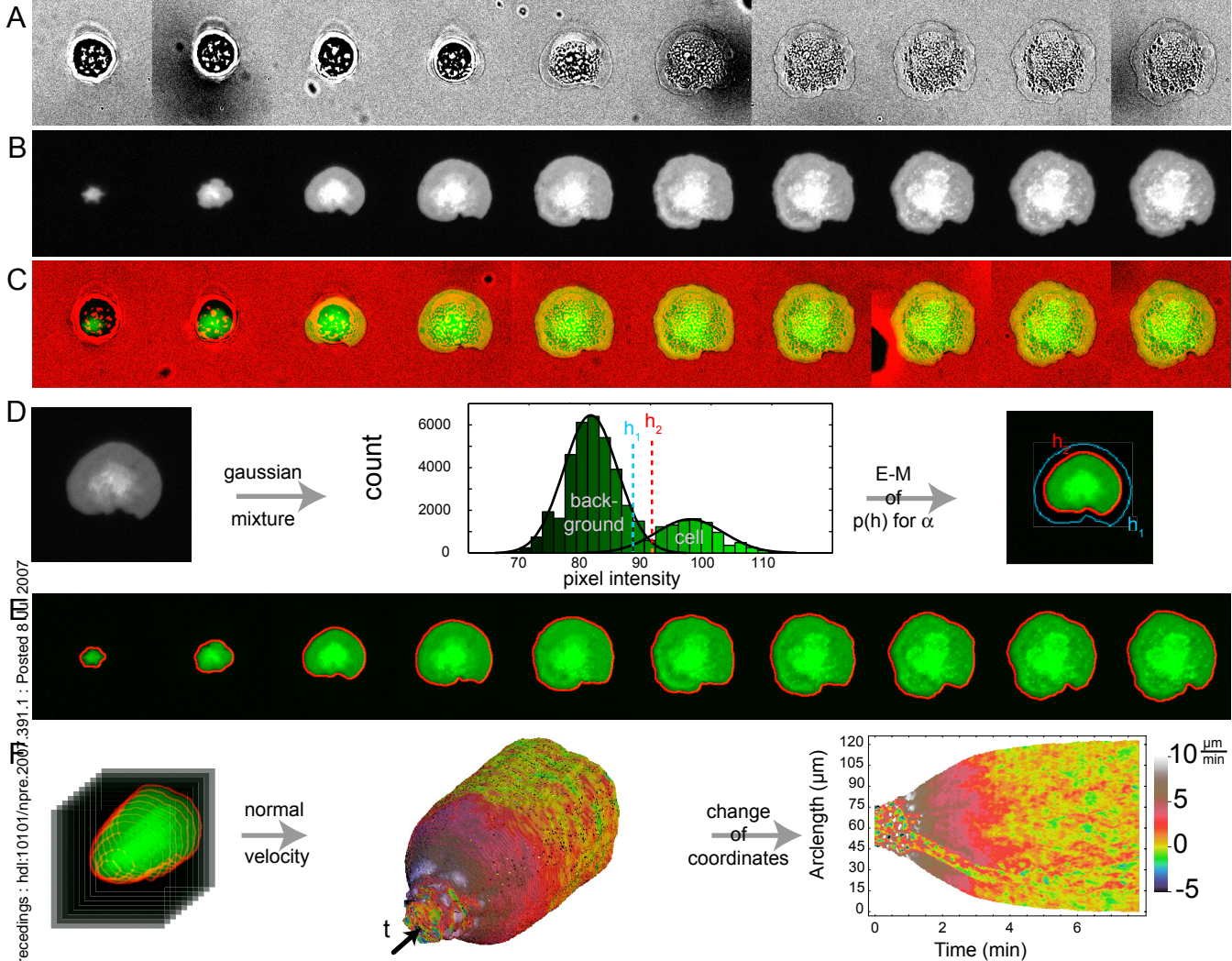
Figure 1: The velocity map encapsulates the kinematics of cell spreading
(A) Bright field sequence of a mouse embryonic fibroblast spreading on a fibronectin coated coverglass. Each image is 62µm high and there is 1 minute between each frame. (B) Same as A except with total internal reflection fluorescence (TIRF) illumination. TIRF reveals only the regions of the cell in closest contact with the surface, allowing for the visualization of edge dynamics at the earliest times. (C) Merge of bright field (red) and TIRF (green) sequences. The cell edge in bright field exactly matches the cell edge in TIRF. (D) Example of Gaussian mixture modeling and expectation-maximization method for image segmentation of a TIRF image (left). A mixture of two Gaussian distributions is used to fit the pixel intensity histogram (middle), where one Gaussian models background pixels and one models pixels corresponding to our fluorescent signal. A threshold is determined by tuning the relative probability that a given pixel intensity belongs to the background or signal distributions (right). The only free parameter in this calculation, performed by a convergent expectation-maximization algorithm, is ?, the tightness factor. Two different values of ? result in two different values for the threshold, h1 and h2. (E) Segmentation of the sequence of TIRF images in B for constant ?. (F) The sequence of contours gives edge position as a function of arc-length and time (left). The edge position is then used to determine the points at which to calculate a 3D optical flow from the original image data (middle). The velocity surface is plotted over arc-length and time (right). The cell analyzed in this figure corresponds to cell 646 in the database.
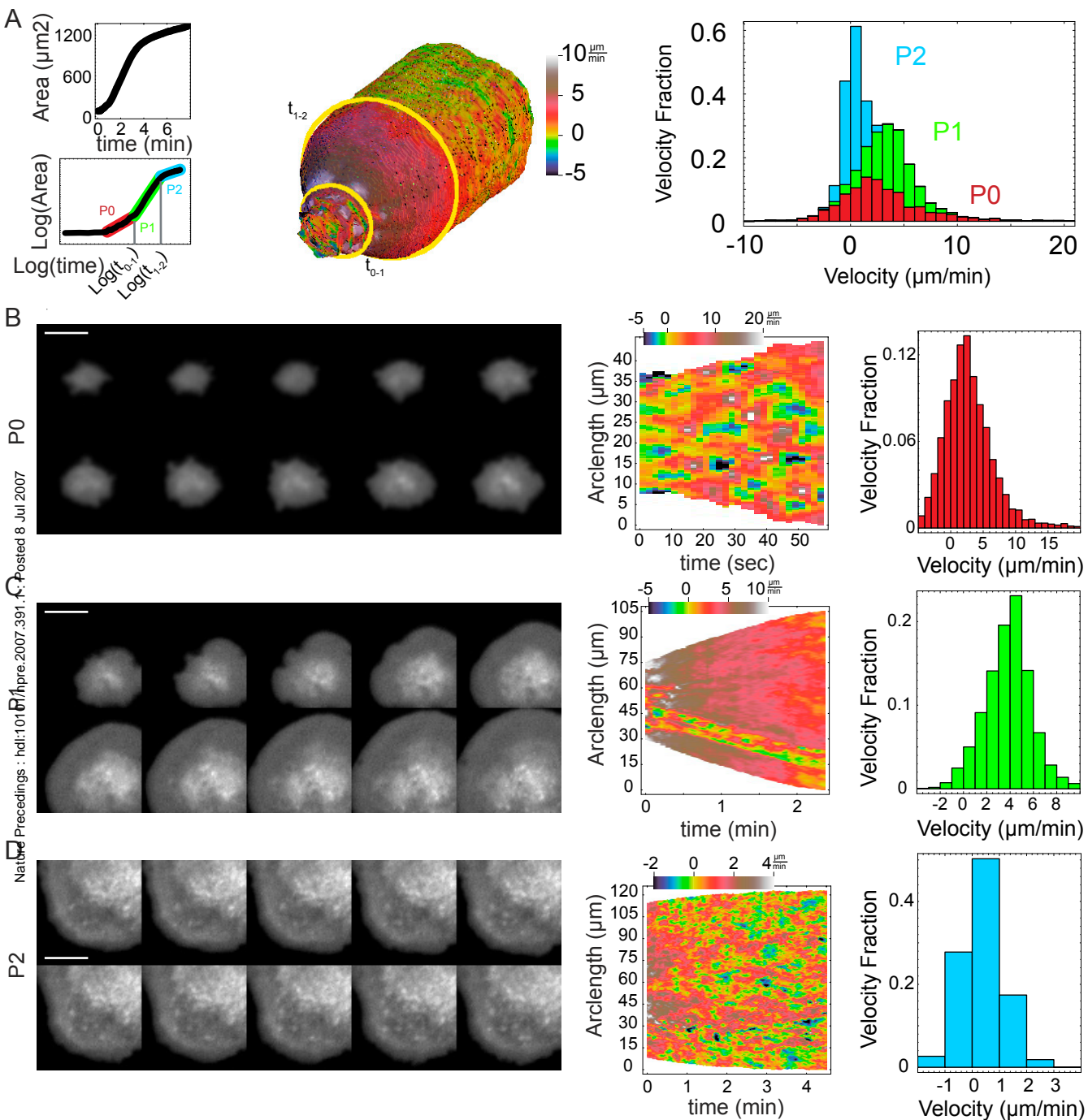
Figure 2: Each spreading phase exhibits a unique kinematic signature

(A) The time domains of different phases are determined by the best fit of a 3-regime, piecewise function to the logarithm of the area curve (left). These domains are then used to divide the velocity map into different regions (middle). The three phases have distinct normal velocity distributions (right). (B) Phase 0 spreading. TIRF sequence of images (left) are 6 seconds apart. Velocity map (middle). Velocity histogram (right). (C) Phase 1 spreading. TIRF sequence of images (left) are 14 seconds apart. Velocity map (middle). Velocity histogram (right). (D) Phase 2 spreading. TIRF sequence of images (left) are 14 seconds apart. Velocity map (middle). Velocity histogram (right). Scale bars represent 10μm. The cell analyzed corresponds to ID 646 in the database.
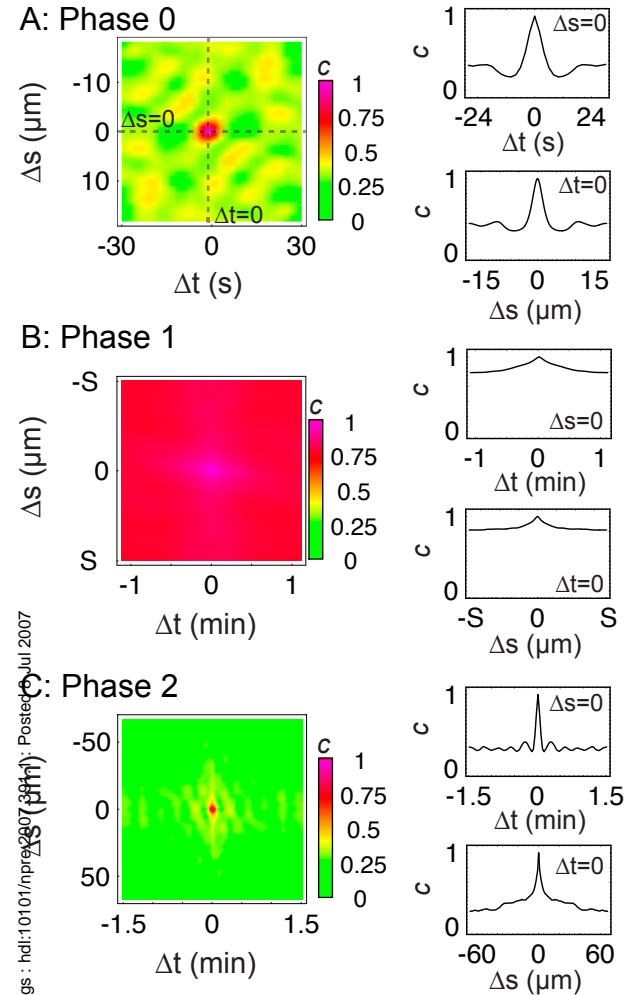
Figure 3: Auto-correlation functions reveal different characteristic lengths and periods in each phase

Two-point correlation function, c(Δt,Δs) applied to velocity maps reveal patterns of membrane movement for P0 (A), P1 (B) and P2 (C). Correlation density maps reveal overall patterns (left column) while plots of the Δt=0 or Δs=0 sections (right column) illustrate temporal and spatial features alone. The width of the first peak in c around the origin gives the average feature size in time and arc-length for each phase. The distance to the first maximum in the time axis gives the average temporal periodicity of the velocity plot. The distance to the first maximum in the space axis gives the average periodicity in space. Diagonals in the correlation plots reveal lateral propagation of active regions, particularly evident in the P0 plot. Arc-length in P1 is expressed with respect to the maximum arc-length, S, because S(t) is changing rapidly in this phase. Database ID for (A) and (B) is 646, (C) corresponds to ID 625.
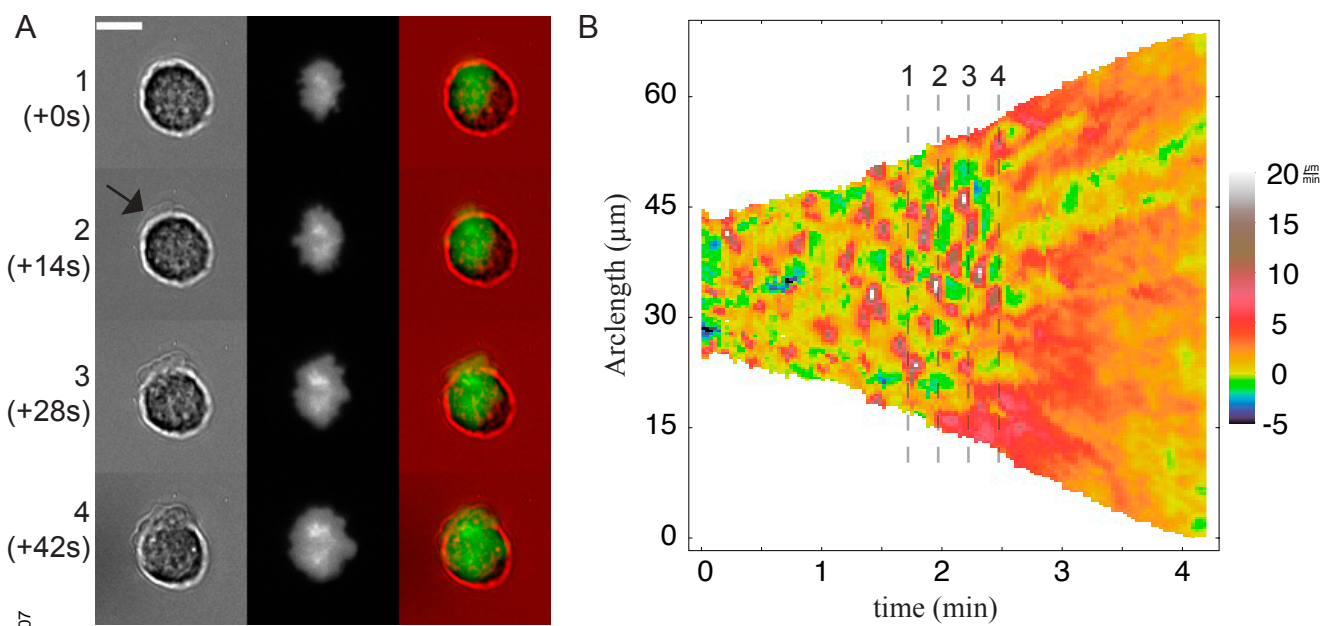
Figure 4 : Periodic protrusion   and retra ction in the basal phase is a result of blebs

 (A) Bright field (left), TIRF (middle) and merge (right) images of a cell exhibiting

blebbing motility (arrow indicates a region of blebbing) during P0. Scale bar is 10µm.

(B) Velocity map of the same cell where the dashed lines indicates the time points

represented by the images in (A). The blebs observed in bright field correspond to the

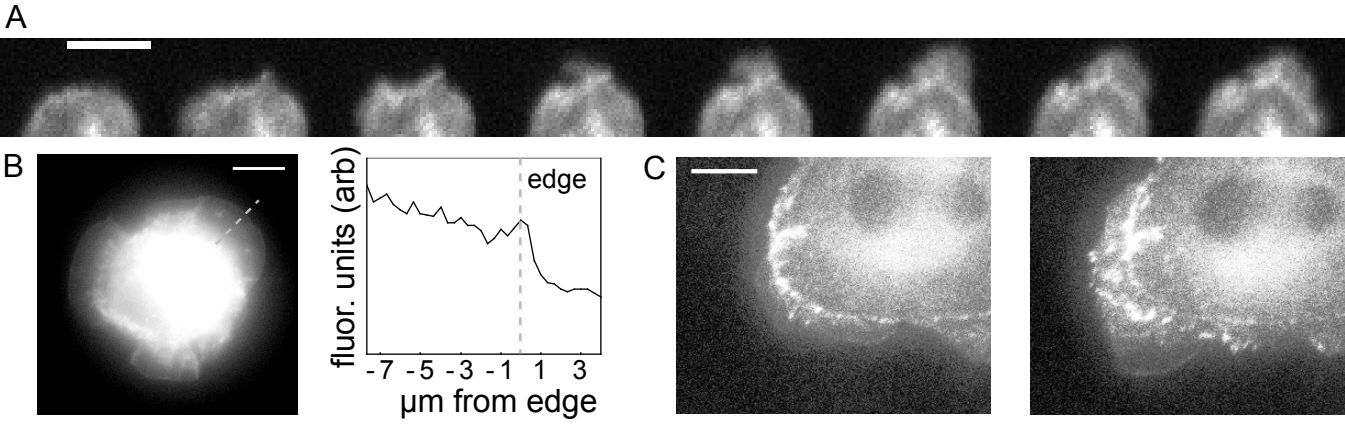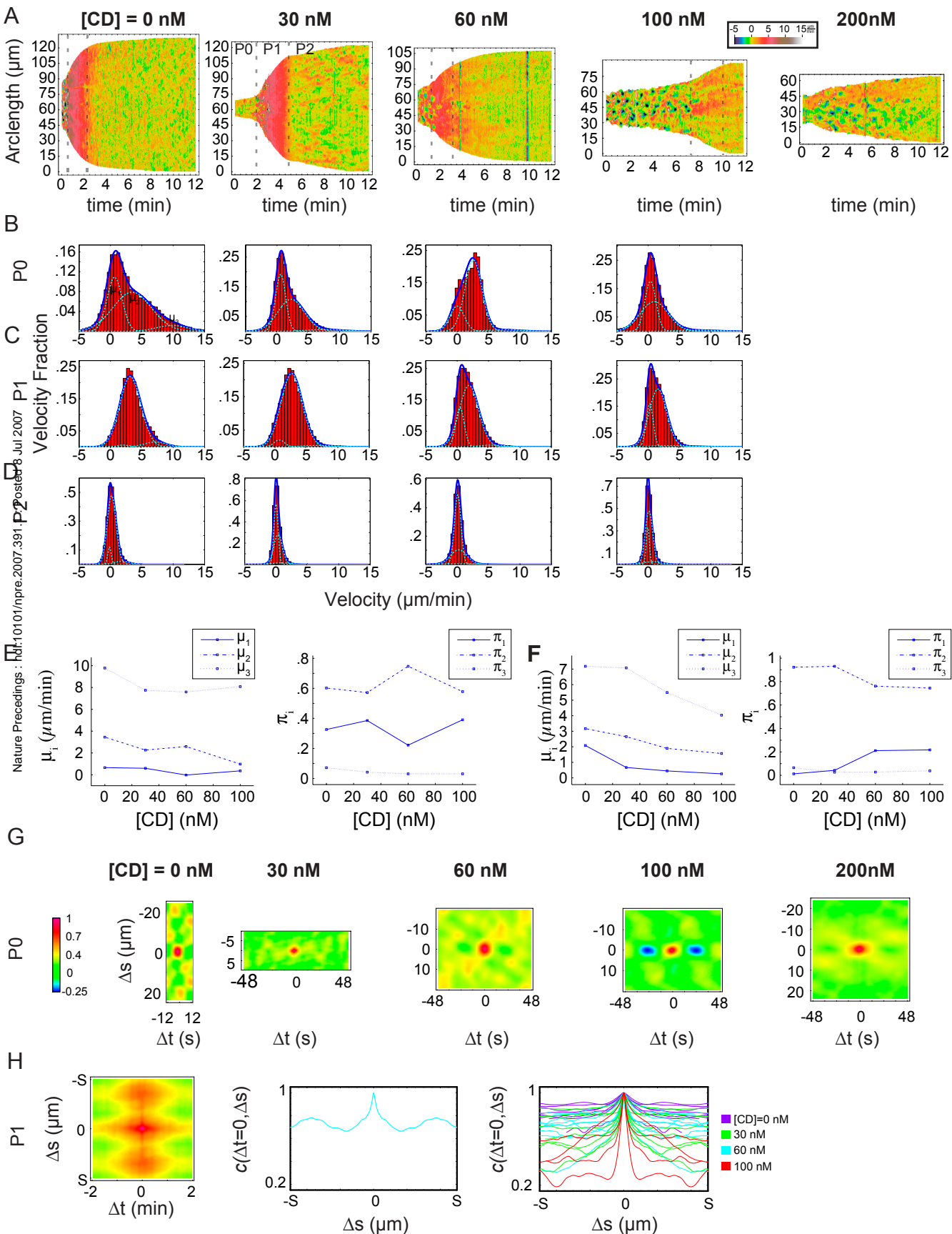regions of patches of protrusion in the velocity map. Cell database ID = 643.

Figure 5: VASP localization acts as a molecular marker to differentiate between the different phases of spreading

(A) A TIRF time sequence of VASP localization reveals that the protein is not enriched at the tips of P0 blebs during protrusion though VASP localizes in adhesions that form following bleb protrusion. (B) During P1, epifluorescence reveals that VASP is concentrated at the leading edge of continuous protrusion, as indicated by a line plot of intensity. The dashed line indicates the region over which the line plot was taken. (C) When the cell enters P2, periodic contractions can occur, with VASP at the tip of the protrusion as well as in rows of adhesions (left). However, the edge can switch back to a continuous protrusion (C, right), at which point VASP is again localized only at the tip, identical to continuous protrusion in P1. Scale bars represent 10μm.

Figure 6: Effect of CD on edge velocity during isotropic cell spreading

Figure 7: Laterally propagating domains of periodic contractions

(A) After entering P2, some cells exhibit a lateral propagation of regions exhibiting periodic contractions. This large scale lateral propagation is seen by correlation analysis (B) performed in the region of the velocity map indicated by the dashed grey lines. After 8 minutes, the speed of lateral propagation decreases (C). The suppression of lateral propagation may be an important step in establishing polarization.

Supporting Material

Movie S1 (Re: Figure 1):

A time-lapse of bright field (red), TIRF (green) micrographs and their overlay (right) shows an immortalized mouse embryonic fibroblast spreading onto a fibronectin coated cover glass.

Movie S2 (Re: Figure 1):

Our algorithms calculate the contour position and the velocity in the direction of the normal to the contour during spreading. The TIRF sequence of an isotropic spreading cell with the contour position overlaid illustrates our technique (left). Each point on the contour is colored to represent the velocity in the direction of the normal to the cell edge at that point (see Fig. 2 for color scale). By stretching out and placing each contours in sequence, we generate the basic unit of our quantitative analysis of cell motility, the velocity map (right). The vertical bars indicate the progression of time.

Movie S3 (Re: Figure 4):

Bright field (left) TIRF (center) and merged (right) images of an isotropic spreading immortalized mouse embryonic fibroblast cell exhibiting P0 blebbing motility. Scale bar represents 5 μm. Frames were collected every two seconds and the display rate is 30 frames per second.

Movie S4 (Re: Figure 5):

TIRF movie of GFP-VASP (left) and DIC (right) exhibit periodic contractions and continuous protrusion in P2 of spreading. Scale bar represents 10 μm.
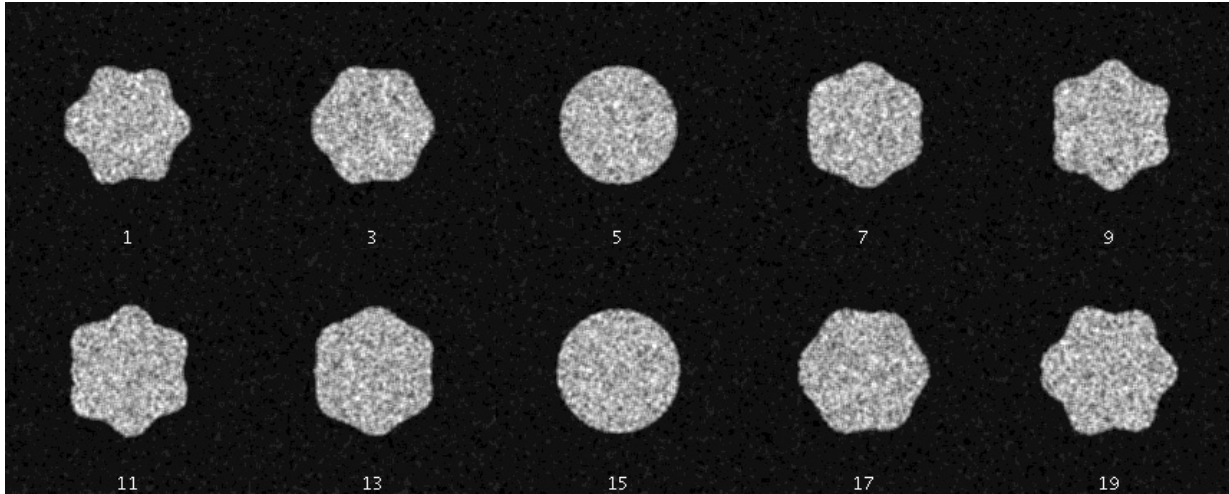
Figure S1 (Re: Figure 4)

(A) Synthetic frames mimic the movements of the real cell edge as observed in TIRF. (B) Velocity map of the synthetic data and (C) histogram of measured velocities. (D) Correlation analysis reveals the spatial and temporal extent of regions of motile activity as well as the spatial and temporal spacing between regions of activity.
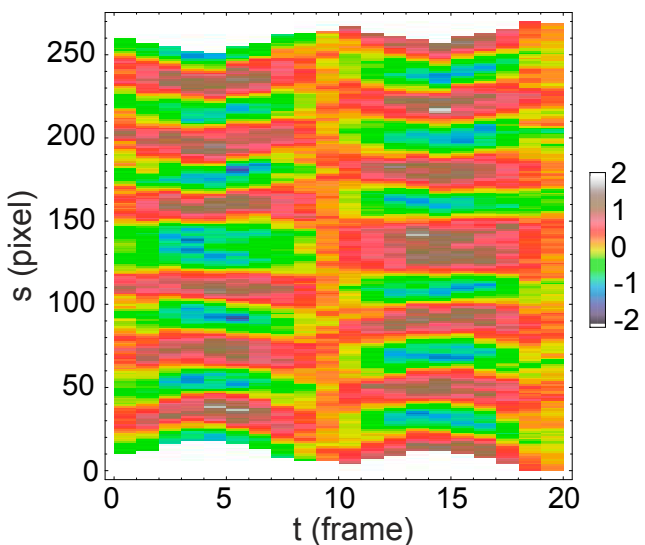
Figure S2, in two parts (Re: Figure 7)

Velocity maps of isotropic cells used in the CD spreading dependence studies. The numbers above each plot indicates the cell ID # in our database. The data for these plots as well as area curves are accessible through our online database.
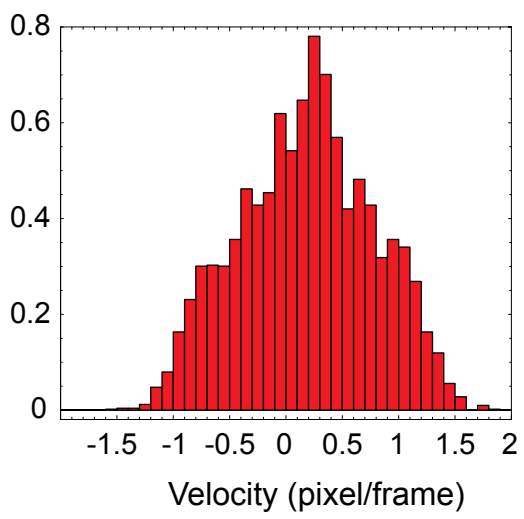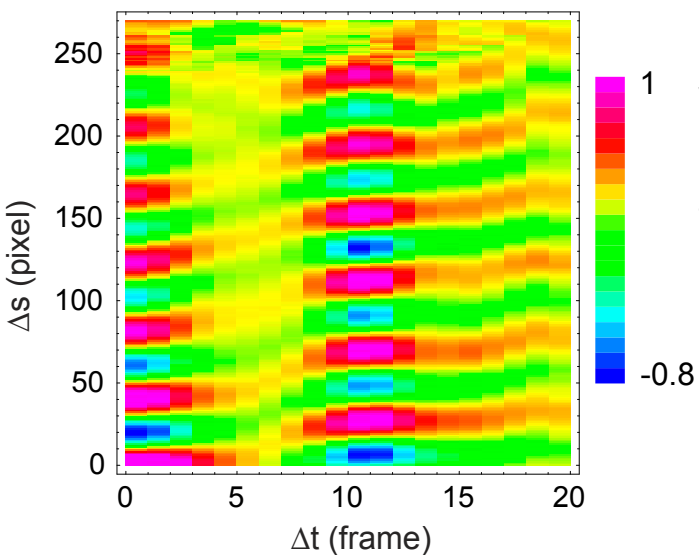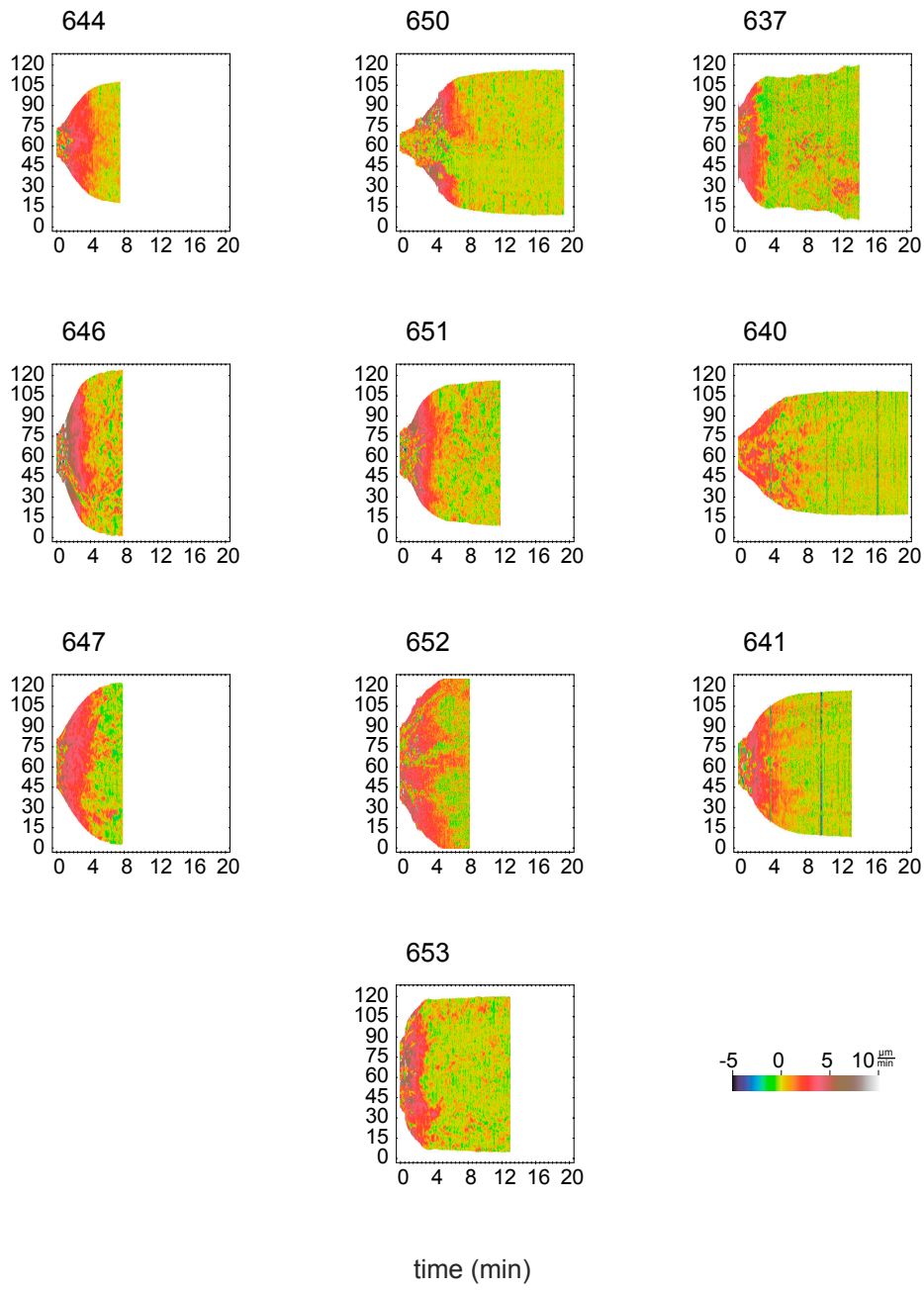
Figure S1 (Re: Figure 4)
(A) Synthetic frames mimic the movements of the real cell edge as observed in TIRF. (B) Velocity map of the synthetic data and (C) histogram of measured velocities. (D) Correlation analysis reveals the spatial and temporal extent of regions of motile activity as well as the spatial and temporal spacing between regions of activity.

[CD] = 0 nM   **30 nM**   **60 nM**   **100 nM**

time (min)

Figure S2, in two parts (Re: Figure 7)

II

[CD] = 0 nM   **30 nM**   **60 nM**

644   650   637

646   651   640

647   652   641

653

-5   0   5   10 $\frac{\mu m}{min}$

time (min)

Arclength (µm)

Figure S2, in two parts (Re: Figure 7)
Velocity maps of isotropic cells used in the CD spreading dependence studies. The numbers above each plot indicates the cell ID # in our database. The data for these plots as well as area curves are accessible through our online database.